Supporting Information

Cluster-like Mo_2N anchoring on reduced graphene oxide as the efficient and deep-degree oxidative desulfurization catalyst

Weizhuang Song,[a] Dongxu Wang,*[a] Xianyun Yue,[a] Chengxu Jin,[a] Yangchen Wu,[a] Yu Shi,[a] Jiancong Liu,[a] Aiping Wu,[a] Chungui Tian*[a] and Honggang Fu*[a]

Key Laboratory of Functional Inorganic Material Chemistry, Ministry of Education of the People's Republic of China, Heilongjiang University. Harbin 150080, China
E-mail: wangdongxu@hlju.edu.cn, tianchungui@hlju.edu.cn, fuhg@hlju.edu.cn

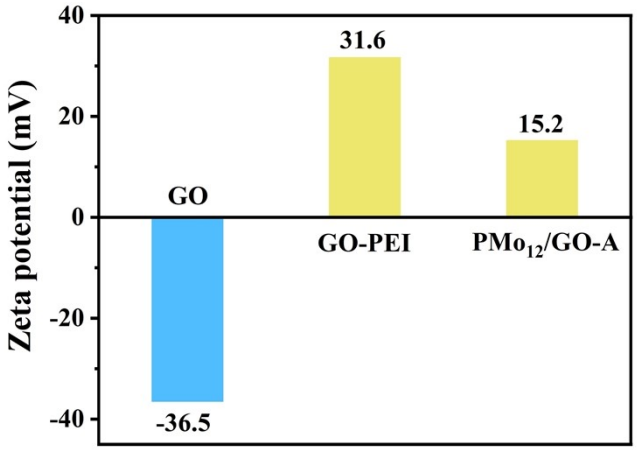

Figure S1. Zeta potentials of GO, GO-PEI and PMo_{12}/GO-A samples.

The zeta potential measurement can provide direct evidence about the change in the surface charge of GO before and after PEI modification (Fig. S1). GO surface is electronegative due to the presence of abundant oxygen-containing functional groups (zeta potential value is -36.5 mV). After PEI modification, the zeta potential value of GO-PEI sample is 31.6 mV, which indicates that the amine groups of PEI successfully combine to the oxygen-containing functional groups of GO thus change the surface charge properties of GO. Finally, the electronegative PMo_{12} groups can be adsorbed on the electropositive GO-PEI surface via electrostatic interactions, resulting in a zeta potential value of 15.2 mV due to the excess of PEI.

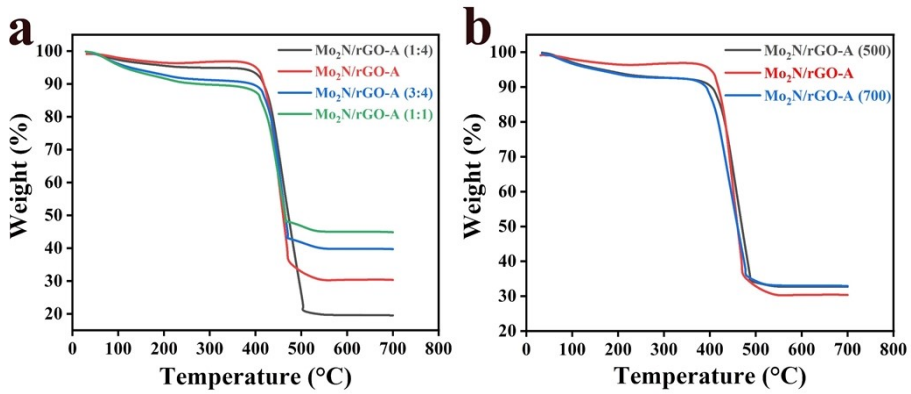

Figure S2. TG curves of the samples (a) prepared with different initial mass ratios of PMo_{12} and GO and (b) prepared with different nitriding temperatures.

Table S1. TGA analysis of Mo_2N/rGO-A (1:4), Mo_2N/rGO-A, Mo_2N/rGO-A (3:4) and Mo_2N/rGO-A (1:1).

Sample	Mass fraction at 350 °C / %	Mass fraction at 580 °C / %	Mass fraction difference / %	Theoretical mass fraction (Mo_2N) / %	Actual mass fraction (Mo_2N) / %
Mo_2N/rGO-A (1:4)	94.90	19.60	75.30	14.48	14.76
Mo_2N/rGO-A	96.80	30.40	66.40	25.29	22.46
Mo_2N/rGO-A (3:4)	91.20	39.80	51.40	33.68	31.21
Mo_2N/rGO-A (1:1)	89.50	45.02	44.03	40.37	35.98

Table S2. TGA analysis of Mo_2N/rGO-A (500), Mo_2N/rGO-A and Mo_2N/rGO-A (700).

Sample	Mass fraction at 350 °C / %	Mass fraction at 580 °C / %	Mass fraction difference / %	Theoretical mass fraction (Mo_2N) / %	Actual mass fraction (Mo_2N) / %
Mo_2N/rGO-A (500)	92.54	32.70	59.84	25.29	25.28
Mo_2N/rGO-A	96.80	30.40	66.40	25.29	22.46
Mo_2N/rGO-A (700)	92.55	33.05	59.50	25.29	25.54

We have determined quantitative results of the Mo_2N component in these samples based on TG analyses (Fig. S2 and Table S1-S2). From TG test in air, we can see a loss

weight of sample at ~420 °C, which can be ascribed to the decomposition of rGO support. In the progress of the calcination, the Mo_2N component in the composites can be converted into MoO_3 in company with the formation of carbon oxide gases by the reaction of the carbon with O_2. The carbon oxide gases are released and the MoO_3 components stay as solid in the system (crucible). We can obtain the content of Mo_2N in the composites based on the amount of MoO_3 by TGA analysis. The content of Mo_2N in the sample was calculated according to the below equation:

Mo_2N % = MoO_3 %×206/144*2*(Mo_2N+rGO) %

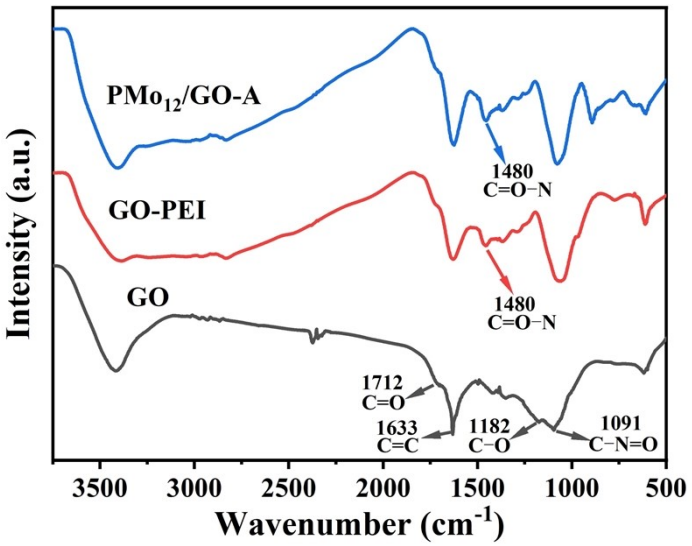

Figure S3. IR spectra of GO, GO-PEI and PMo_{12}/GO-A samples.

The Fourier transform infrared (FT-IR) spectra of samples at the different steps are shown in Fig S3. In the GO spectrum, the characteristic absorbance bands at 1633 and 1091 cm^{-1} can be ascribed to C=C and O=N-C, respectively. The peaks at 1712 and 1182 cm^{-1} correspond to C=O and C-O stretch from the oxygen-containing groups of GO. The peak of C=O-N (1480 cm^{-1}) can be found in the FT-IR spectrum of GO-PEI and PMo_{12}/GO-A, indicating that the amine groups from PEI are successfully grafted on the GO. In addition, for GO-PEI and PMo_{12}/GO-A, the characteristic absorbance bands of C=O and C-O stretch become weak, which may be due to the combination of the amine groups with the oxygen-containing groups, and the covering effect of PEI on GO.

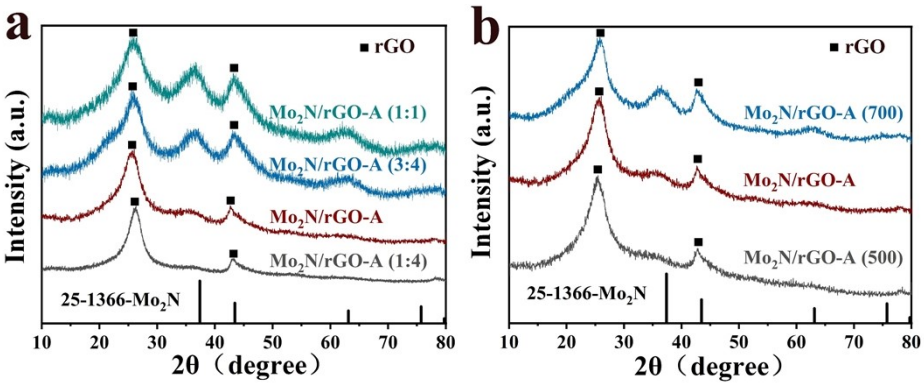

Figure S4. XRD patterns of the samples (a) prepared with different initial mass ratios of PMo_{12} and GO and (b) prepared with different nitriding temperatures.

The XRD patterns (Fig. S4a) indicate that the peak intensity of Mo_2N component increases with the increasing the amount of PMo_{12}, indicating the contents and compositions can be controlled by changing the initial ratio of PMo_{12} and GO. In addition, the relatively broad diffraction peaks still prove the characteristics of small size and high dispersion of Mo_2N on rGO. Fig. S4b shows that the diffraction peaks of Mo_2N are extremely weak when the nitriding temperature is 500 °C, indicating the poor crystallinity of Mo_2N phase. When the nitriding temperature is raised to 700 °C, Mo_2N diffraction peaks become stronger, which means the increase of crystallinity. Moreover, it's worth noting that the broad diffraction peaks for Mo_2N/rGO-A (700) also show the relatively small size of Mo_2N particles. The result shows that the nitriding temperature is a key factor affecting the crystallinity of Mo_2N, but has a little effect on its size.

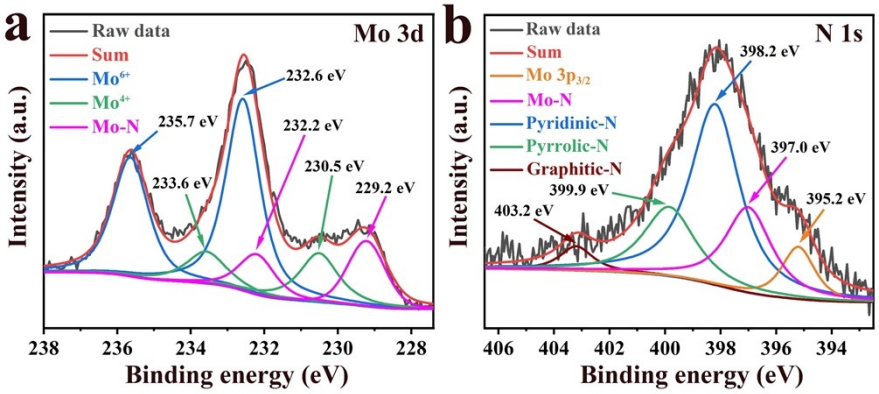

Figure S5. The high-resolution XPS spectra of (a) Mo 3d and (b) N 1s for Mo_2N/rGO-D.

The high-resolution XPS spectra (Fig. S5a) of Mo 3d shows the presence of Mo in the form of Mo-N bonds, Mo^{4+} and Mo^{6+}, in which the two peaks at 229.2 and 232.2 eV attributed to Mo-N $3d_{5/2}$ and $3d_{3/2}$, respectively. And the peaks at 230.5/233.6 eV and 232.6/235.7 eV are attributed to Mo^{4+} and Mo^{6+} species, which is due to the surface oxidation of Mo_2N particles in the air. The N 1s XPS spectra (Fig. S5b) shows the peak located at 397.0 eV suggest the formation of Mo-N bond, the peaks for pyridinic-N (398.2 eV), pyrrolic-N (399.9 eV) and graphitic-N (403.2 eV) indicating N doping, and the peak located at 395.2 eV can be attributed to the binding energy of Mo $3p_{3/2}$.

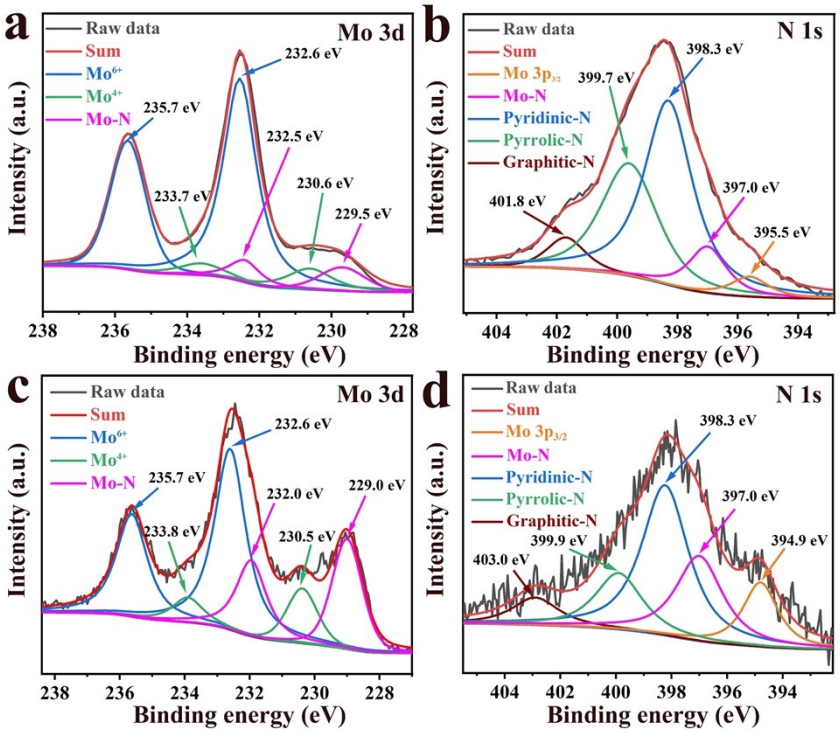

Figure S6. The high-resolution XPS spectra of Mo 3d and N 1s for (a)-(b) Mo_2N/rGO-A (500) and (c)-(d) Mo_2N/rGO-A (700).

Fig. S6 shows the high-resolution XPS spectra of Mo 3d and N 1s for Mo_2N/rGO-A (500) and Mo_2N/rGO-A (700). The Mo 3d and N 1 s XPS spectra of Mo_2N/rGO-A (500) and Mo_2N/rGO-A (700) samples both display the presence of Mo-N bonds, verifying the formation of Mo_2N. With the increase of nitriding temperature, the intensity of XPS peaks corresponding Mo-N bonds is stronger gradually, meaning the increased crystallinity of Mo_2N, which is agreed well with XRD observation.

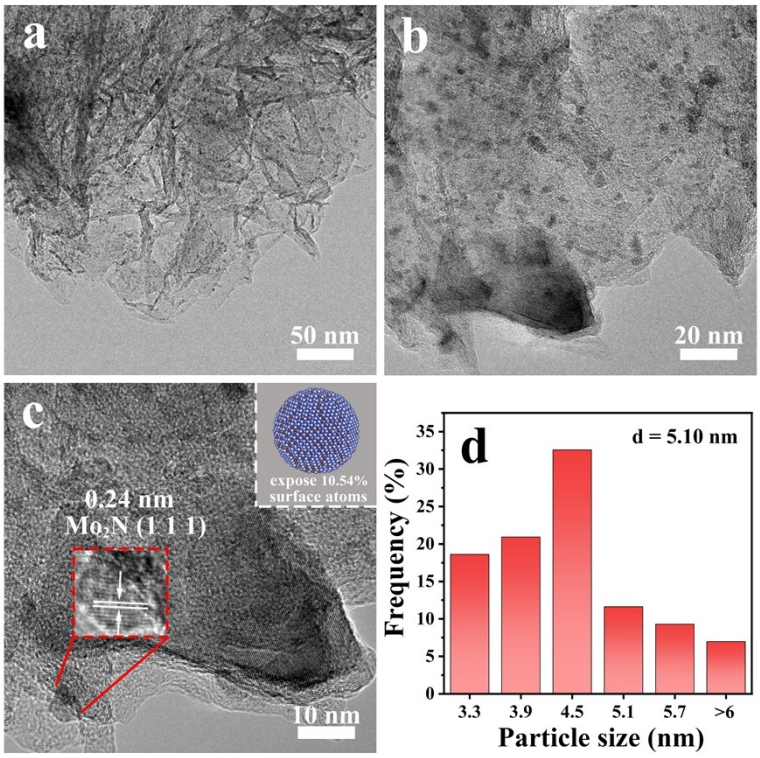

Figure S7. (a)-(c) TEM images of Mo_2N/rGO-D sample, inset in (c) is 5.1 nm Mo_2N particle model, and (d) the size distribution of the Mo_2N particles for Mo_2N/rGO-D sample.

Fig. S7 shows the TEM images of the Mo_2N/rGO-D catalyst and the size distribution of the Mo_2N particles for Mo_2N/rGO-D. In TEM observations, the Mo_2N with larger size and high stacking were dispersed on rGO surface, this may be due to the weak interaction between metal species and rGO. The particle size distribution result shows that the average size of the Mo_2N particles is 5.10 nm for Mo_2N/rGO-D sample. Some large-sized aggregations larger than 25 nm can also be seen. Above results also demonstrate the important role of PEI-anchoring strategy in inhibiting the aggregation of the metal species. Furthermore, the surface atom exposure rate of Mo_2N particle is also calculated. The 5.1 nm Mo_2N particle model has a total atom of 6120 and a surface atomic number of 645, expose 10.54% surface atoms. The surface atom exposure rate of Mo_2N particle model (1.5 nm) can reach 35.90%, much exceeding large-sized Mo_2N particle model of 5.1 nm. This suggests that the Mo_2N/rGO-A can expose more surface active sites than the Mo_2N/rGO-D, which is conducive to the improvement of catalytic performance.

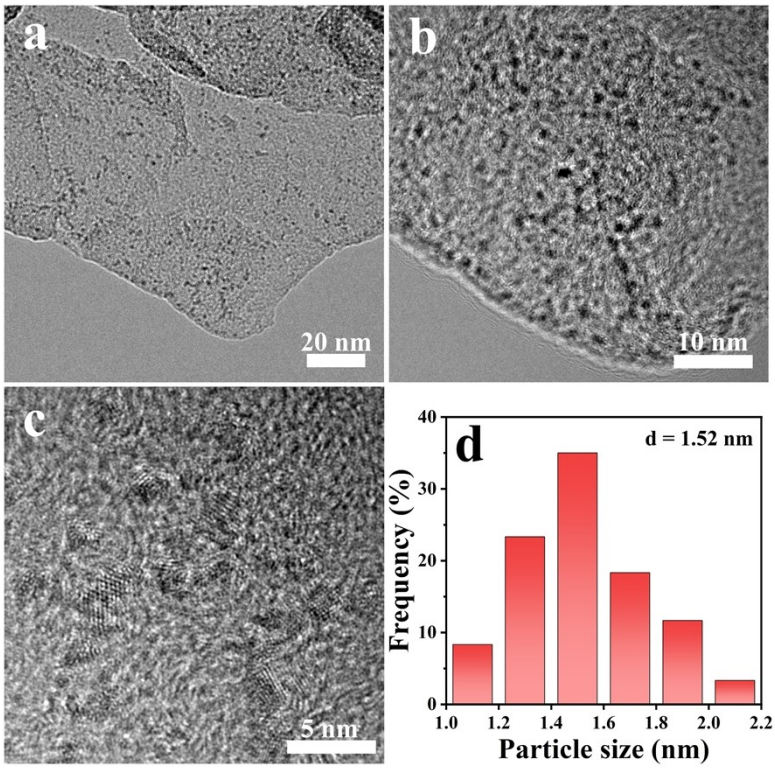

Figure S8. (a)-(c) TEM images of Mo_2N/rGO-A (500) sample and (d) the size distribution of the Mo_2N particles for Mo_2N/rGO-A (500) sample.

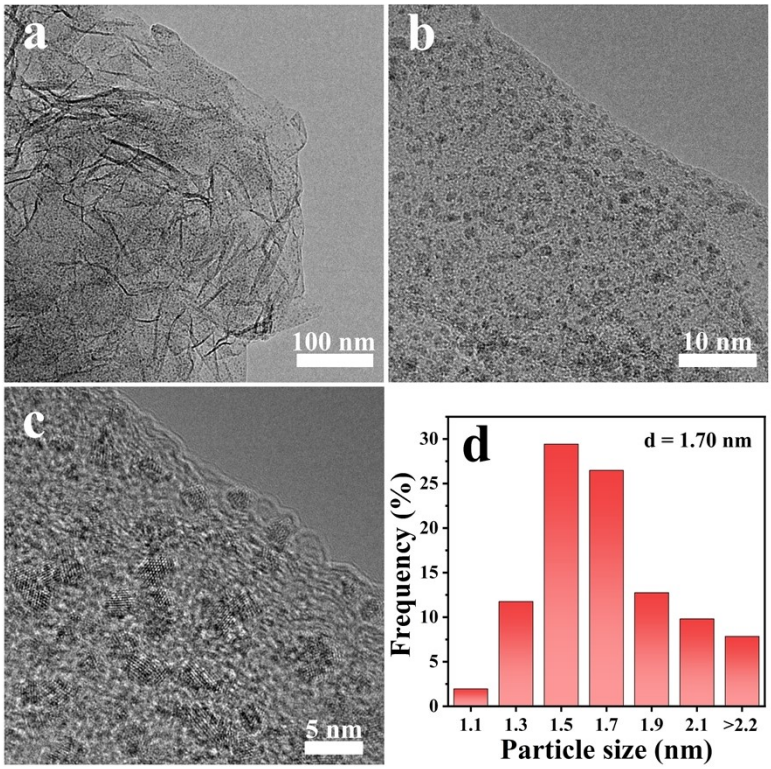

Figure S9. (a)-(c) TEM images of Mo_2N/rGO-A (700) sample and (d) the size distribution of the Mo_2N particles for Mo_2N/rGO-A (700) sample.

Fig. S8 and Fig. S9 show the TEM images of the Mo_2N/rGO-A (500) and Mo_2N/rGO-A (700) catalyst and the size distribution of the Mo_2N particles. From the TEM images, it can be observed that the lattice fringes of Mo_2N particles become gradually clear with the increase of nitriding temperature, showing the increase of crystallinity. The particle size distribution results show that the average sizes of Mo_2N particles are 1.52 nm, 1.70 nm for Mo_2N/rGO-A (500) and Mo_2N/rGO-A (700) samples, which indicates that the nitriding temperature has a little effect on the size of Mo_2N particles. This also demonstrates the effectiveness of the PEI-anchoring strategy in controlling particle size and dispersion.

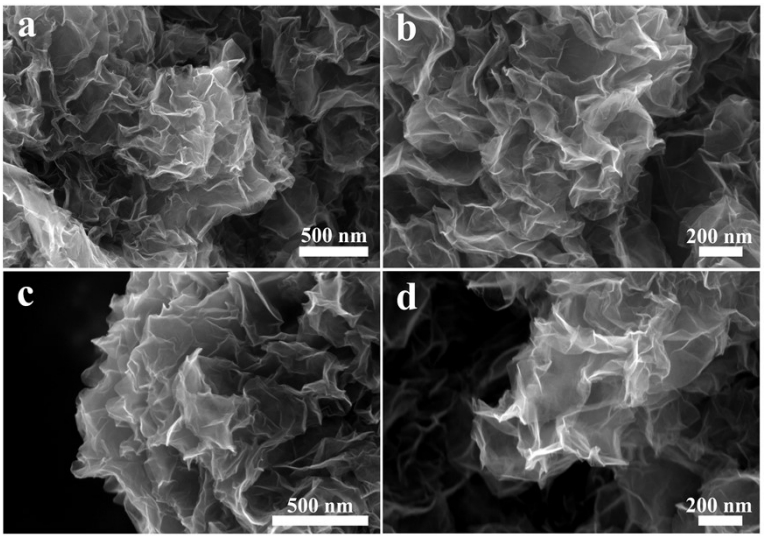

Figure S10. SEM images of the samples prepared with different nitriding temperatures: (a)-(b) Mo_2N/rGO-A (500) and (c)-(d) Mo_2N/rGO-A (700).

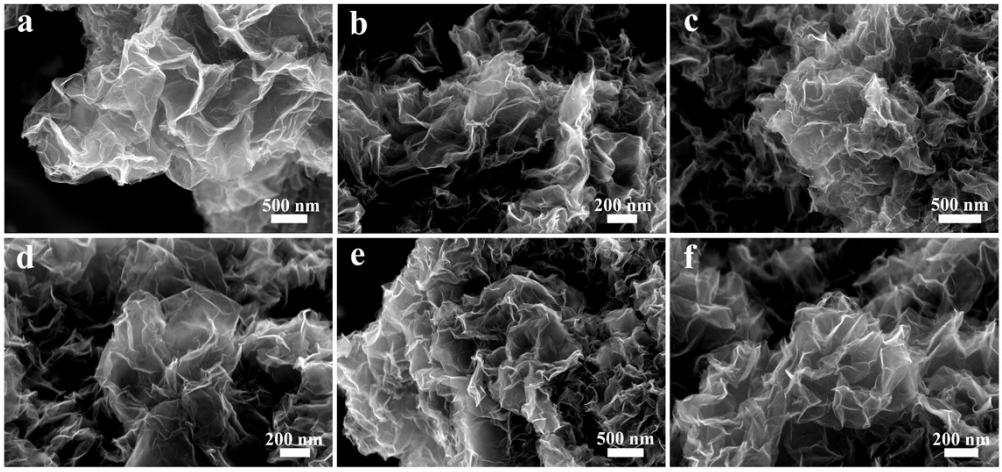

Figure S11. SEM images of the samples with different mass ratios of PMo_{12} and GO: (a)-(b) Mo_2N/rGO-A (1:4), (c)-(d) Mo_2N/rGO-A (3:4) and (e)-(f) Mo_2N/rGO-A (1:1).

Fig. S10 and Fig. S11 show the SEM images of the samples prepared with different nitriding temperatures (Mo_2N/rGO-A (500) and Mo_2N/rGO-A (700)) and prepared with different mass ratios of PMo_{12} and GO (Mo_2N/rGO-A (1:4), Mo_2N/rGO-A (3:4), Mo_2N/rGO-A (1:1)). We can see the same 2D ultra-thin structure as the Mo_2N/rGO-A catalyst.

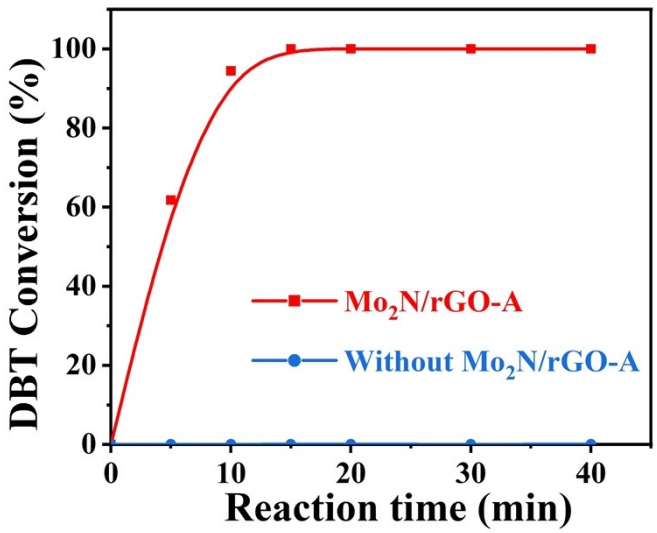

Figure S12. Comparison of DBT conversion over Mo_2N/rGO-A and without Mo_2N/rGO-A in the H_2O_2-containing systems.

In order to verify the importance of Mo_2N/rGO-A catalyst in the reaction, the ODS reaction without Mo_2N/rGO-A catalyst was tested in the optimal reaction conditions. As shown in Fig. S12, almost no conversion of DBT in the absence of Mo_2N/rGO-A catalyst. Therefore, the ODS reaction could not occur without the addition of catalyst in the H_2O_2-containing system.

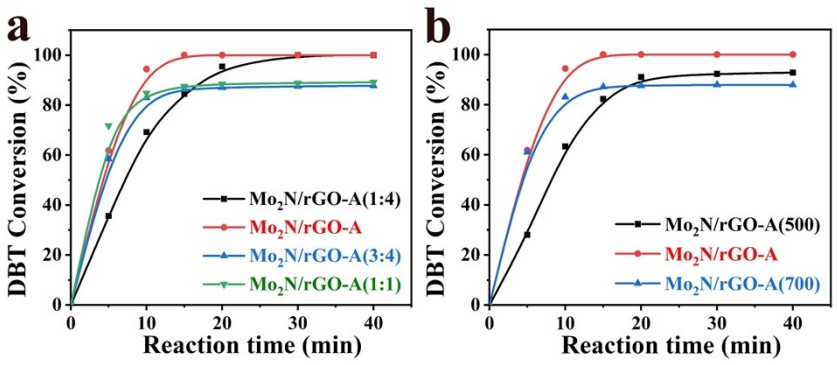

Figure S13. Comparison of DBT conversion over (a) the samples prepared with different initial mass ratios of PMo_{12} and GO and (b) the samples prepared with different nitriding temperatures of Mo_2N/rGO (Oxidation condition: 1000 mg L^{-1} DBT, O/S ratio:10, catalyst: 20 mg, temperature: 60 °C, time: 40 min, mixing speed: 500 rpm).

As shown in Fig. S13a, the conversion of DBT within 20 min: Mo_2N/rGO-A (3:4) < Mo_2N/rGO-A (1:1) < Mo_2N/rGO-A (1:4) < Mo_2N/rGO-A, indicating that the increase in the loading of the active species does not necessarily improve the activity of the catalyst. Moderate loading of Mo species facilitates high dispersion of active centers, which plays an important role in improving the efficiency of desulphurization. Although the DBT in the Mo_2N/rGO-A (1:4) system had been basically converted completely within 30 min, the conversion rate of the Mo_2N/rGO-A system was faster compared with that of Mo_2N/rGO-A (1:4). Therefore, Mo_2N/rGO-A was chosen as the catalyst for the ODS reaction due to its good performance and resources saving.

The activities of the catalysts Mo_2N/rGO-A obtained at different nitriding temperatures were compared. As shown in Fig. S13b, the initial reaction rate gradually increased with the increase of nitriding temperature, and the conversion of DBT within 20 min: Mo_2N/rGO-A (700) < Mo_2N/rGO-A (500) < Mo_2N/rGO-A. It can be seen that higher or lower nitriding temperature will lead to a decrease in catalytic activity, so 600 °C was chosen as the optimum nitriding temperature.

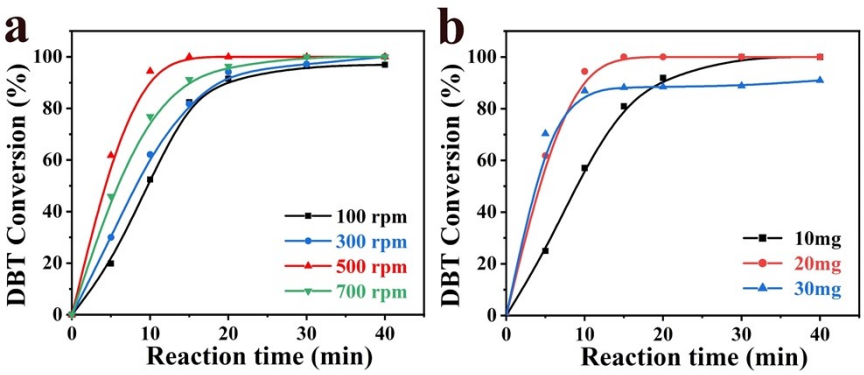

Figure S14. Effect of (a) mixing speed (rpm) and (b) dosage of catalyst for the conversion of DBT over the Mo_2N/rGO-A catalyst.

To understand the effect of diffusivity on the ODS reaction, the effect of different stirring speeds (rpm) on the conversion of DBT was investigated in the presence of Mo_2N/rGO-A catalyst. As shown in Fig. S14a, the initial reaction rate increases with the increase of stirring speed, but the initial reaction rate decreases instead at 700 rpm. Therefore, it can be concluded that slower or faster stirring speeds were not conducive to the contact between the surface active sites and the reactants, which leads to a decrease in performance or a decrease in the reaction rate, so 500 rpm was finally chosen as the optimal stirring speed.

The effect of the amount of Mo_2N/rGO-A catalyst on the ODS reaction was investigated. As shown in Fig. S14b, the catalytic rate was obviously accelerated with the increase of catalyst mass, but after reaching a certain level, increasing the amount of catalyst instead decreased the DBT conversion. This may be due to the fact that more catalyst reacted with H_2O_2 and the decomposition of H_2O_2 was accelerated, resulting in insufficient H_2O_2 content, so 20 mg was chosen as the optimum catalyst mass.

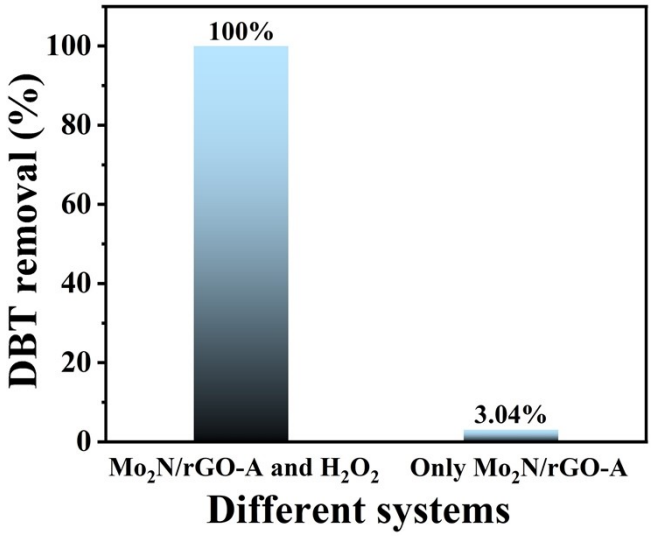

Figure S15. Comparison of DBT removal over oxidation (Mo_2N/rGO-A and H_2O_2) and adsorption (only Mo_2N/rGO-A) at 40 min.

To verify the adsorption of DBT on Mo_2N/rGO-A, the adsorption experiment (only Mo_2N/rGO-A) was done in the optimal reaction conditions. As shown in Fig. S15, the efficiency of DBT removal by adsorption was much lower than that by oxidation at 40 min. The result showed that the adsorption of the Mo_2N/rGO-A catalyst to the DBT was negligible, the reduction of sulfur content in the reaction system was attributed to the conversion of reactants under the action of catalyst.

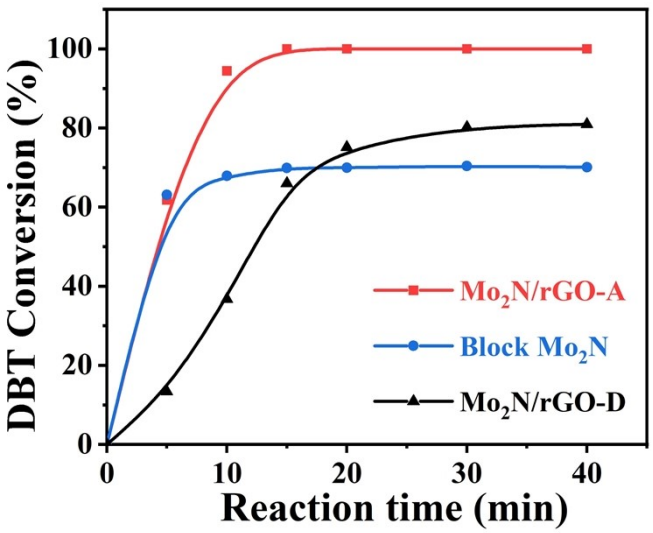

Figure S16. Comparison of DBT conversion over Mo_2N/rGO-A, Mo_2N/rGO-D and block Mo_2N catalysts.

In order to further prove the effect of the size of Mo_2N catalyst on its catalytic performance, the unsupported Mo_2N catalyst (block Mo_2N) was prepared and tested in ODS reaction. As shown in Fig. S16, the catalytic performance of block Mo_2N was lower than that of Mo_2N/rGO-A and Mo_2N/rGO-D catalysts in the same reaction conditions. The result further demonstrated the superiority of small-sized Mo_2N in ODS reaction.

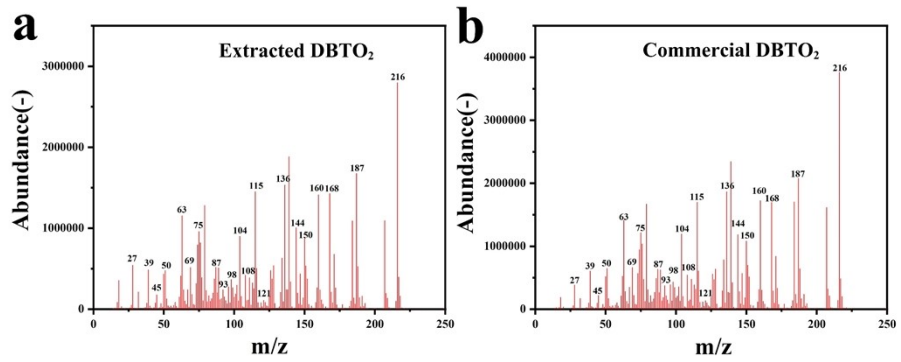

Figure S17. GC-MS analysis of the (a) product extracted in the ODS of DBT and (b) commercial $DBTO_2$.

The oxidation of DBT over the Mo_2N/rGO-A catalyst was confirmed via GC–MS analysis of the acetonitrile phase, collected after the ODS of DBT. As shown in Fig. S17, the oxidized product and commercial $DBTO_2$ have very similar fragmentation patterns to each other, supporting the oxidation of DBT into $DBTO_2$.

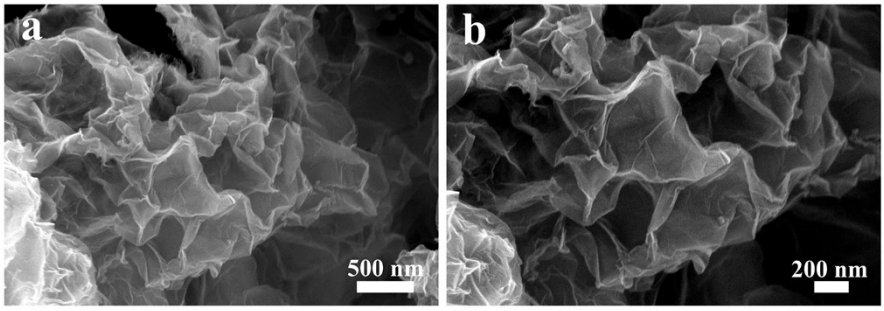

Figure S18. (a)-(b) SEM images of recycled Mo_2N/rGO-A catalyst.

The structure of the recycled Mo_2N/rGO-A catalyst was characterized by scanning electron microscopy (SEM). As shown in Fig. S18 a-b, the recycled Mo_2N/rGO-A catalyst still retained the 2D ultra-thin structure. It was shown that the catalyst of Mo_2N/rGO-A had a very stable structure in ODS even after the successive recycles.